The following publication W. Liu, J. Lu, C. C. Mi and K. T. Chau, "Integrated Sensorless Wireless Charging Using Symmetric High-Order Network for Multistorey Car Parks," in IEEE Transactions on Power Electronics, vol. 39, no. 8, pp. 10568-10581, Aug. 2024 is available at https://doi.org/10.1109/TPEL.2024.3395461.

Integrated Sensorless Wireless Charging Using Symmetric High-Order Network for Multistorey Car Parks

Wei Liu, *Senior Member, IEEE*, Jianghua Lu, *Member, IEEE*, Chunting Chris Mi, *Fellow, IEEE*, and K.T. Chau, *Fellow, IEEE*

Abstract—**For multistorey car parks, this paper proposes and implements an integrated sensorless wireless charging (SWC) system of electric vehicles (EVs) using a symmetric high-order network that is designed to mirror the electrical parameters of the onboard receiver and battery. The proposed SWC control can avoid the need of communicating and sensing the receiver's and battery's states. It possesses the competitive advantages of being controller-free, sensor-free, communication-free, converter-free, and switch-free onboard. Given the efficient charging for millions of EVs, this integrated SWC scheme can effectively reduce the electrical and electronic component counts, which aligns with the themes of carbon neutrality and environmental sustainability. By detecting the current threshold and then switching two resonant frequencies, the symmetric high-order network enables the autonomous management of constant-current and constant-voltage charging modes while maintaining the zero-phase-angle operation. The experimental DC-to-DC efficiency can reach 91.8% based on a 2.4-kW proof-of-concept prototype at a 150-mm transfer distance. Software simulation and hardware experimentation are given to verify the feasibility of proposed integrated SWC system using the symmetric high-order network.**

Index Terms—**Sensorless wireless charging, electric vehicles, multistorey car parks, symmetric network.**

I. INTRODUCTION

ELECTRIC vehicles (EVs), consumer electronics and biomedical implants can continuously benefit from the development of wireless power transfer (WPT) technologies [1]. Generally, WPT has numerous advantages of high flexibility, high mobility and high safety, thanks to the features of waterproof, sparkproof and contactless power delivery [2], [3]. It can not only enable stationary charging conveniently in multistorey car parks (MCPs) but also support wireless charging on-the-go, particularly attractive for EVs [4]. Significantly, the contactless power delivery of WPT can avoid invasive surgeries and ensuing complications during the patients' treatments using medical implants [5]. Recently, new WPT schemes are explored extensively, such as wireless EV energy networks [6], [7], magnetic field editing [8], [9], wireless power and drive transfer [10], energy encryption and modulation [11], and wireless sensor networks [12].

Generally, a whole wireless charging system comprises: 1) batteries and battery management [13]; 2) sensors and communications; 3) charging profile and modulation strategies; and 4) power converters and resonant networks including pads and compensation circuits. Nowadays, state-of-the-art batteries in EVs still ought to be further broken through the technical bottleneck of energy density [14]. Nevertheless, stationary wireless charging significantly improved the convenience of park-and-charge for battery energy refueling [15], while dynamic wireless charging made the scenario of move-and-charge come true [2]. Both solutions aim to alleviate the over-dependence on batteries and lengthen the cruise mileage of EVs. On the other hand, conventional wireless charging schemes [16] were usually deployed with onboard sensors necessary for generating the feedback of charging voltage and current at the receiver side. Moreover, wireless communication was indispensable yet to delivering the feedback that participates in the charging control at the transmitter side. To implement wireless data transfer, the use of communication devices such as Bluetooth, ZigBee or Wi-Fi inevitably suffers from considerable delay and data transfer interval [16], thus disrupting the system stability and demoting control performance. Wireless power and data transfer [17] was another solution to creating a wireless communication channel that can be established separately or jointly with the power channel. However, the hardware and software of modulation and demodulation increase the system complexity. Possible malfunctions of sensors and communications will be disruptive and catastrophic for personal and property security.

Although a constant-power charging profile was actively explored to maximize the battery charging efficiency [18], the constant-current (CC) and constant-voltage (CV) charging [19] is still widely recognized as one of the most efficient and most practical charging profiles. The single-frequency network can generate either CC or CV output but not both unless using real-time feedback and control [19]. However, the double-frequency network has the potential to enable both the CC and CV charging while following the standard of SAE J2954. These two network design approaches are essentially different. On the other hand, various modulation methods can be used

---

This work was partially supported by a grant from the Hong Kong Research Grants Council, Hong Kong Special Administrative Region, China, under Project No. T23-701/20-R, and partially supported by two grants from The Hong Kong Polytechnic University, under Project No. P0048560 and P0048360. (Corresponding author: *K.T. Chau.*)

Wei Liu, and K.T. Chau are with the Research Centre for Electric Vehicles and Department of Electrical and Electronic Engineering, The Hong Kong Polytechnic University, Hong Kong, China. (e-mail: k.t.chau@polyu.edu.hk; wei.liu@polyu.edu.hk).

Jianghua Lu is with the School of Information Science and Engineering, Wuhan University of Science and Technology, Wuhan 430081, China (e-mail: jianghualu@wust.edu.cn).

Chunting Chris Mi is with the Department of Electrical and Computer Engineering, San Diego State University, San Diego, CA 92182 USA (e-mail: cmi@sdsu.edu).

for battery charging management and efficiency optimization, such as pulse width modulation [20], pulse density modulation [21], [22], pulse frequency modulation [23], [24] and their hybrids. Importantly, wide bandgap semiconductor devices are widely identified as a real breakthrough in power electronics because they radically improve the efficiency, power density and high-frequency switching performances of converters [25].

By designing the low-order, high-order and higher-order compensation, the resonant networks of WPT can perform the functions of load-independent CC/CV outputs [26], high-order transformation [23] and zero-voltage-switching realization [27]. Accordingly, general design pathways were summarized in detail to provide guidelines for the selection and design of compensation circuits [28]. Apart from the inductive power transfer, compensation networks were already extended to the exploration of capacitive power transfer [29]. However, all tuning methods are based on the single-frequency network designs, rarely achieving the load-independent CC and CV charging modes in one fixed resonant network except for topology reconfiguration. Very recently, a series of double-frequency resonant networks were actively explored for achieving both the CC and CV charging while maintaining the zero-phase-angle (ZPA) operation [15]. Further explorations were also tried to minimize the component counts without sacrificing any charging performances [30]. The double-frequency modulation of an inductor-capacitor-capacitor (*LCC*)-*LCC* network was reported [31], [32] to support the CC and CV charging for EVs, However, both schemes operated outside the frequency range recommended by the international standard of SAE J2954. With the help of such artful networks, sensorless wireless charging (SWC) technology deserves to be newly explored without the use of onboard sensors, communications, converters, and controllers, especially for the applications of MCPs in urban areas.

For developing autonomous charging technology, this paper proposes an integrated SWC system using a symmetric high-order network for wireless park-and-charging of EVs in the MCPs, as shown in Fig. 1. This scheme enables onboard communication-free, sensor-free, controller-free, converter-free and switch-free, forming competitive configurations. All these benefits are highly desirable by MCPs towards carbon neutrality and sustainable development. Detection of a current threshold at the transmitter side only can readily determine the transition point of switching between the CC and CV modes while keeping the ZPA operation, thus successfully managing the integrated SWC in the MCPs.

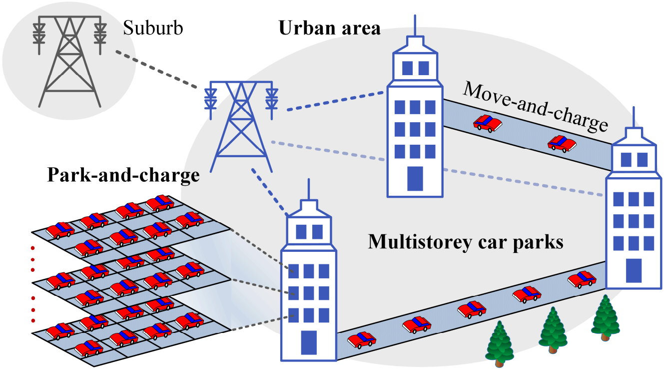

Fig. 1. Schematic of integrated SWC in MCPs.

Section II will introduce the proposed integrated SWC system. Section III will discuss the system superiority and insensitivity of the proposed SWC technology. In Section IV, the secondary sensorless charging control will be delineated to realize a reliable SWC by detecting the current threshold and switching the operating frequencies. In Section V, simulation verification will be performed, and a proof-of-concept prototype will be constructed and tested to verify the proposed integrated SWC system using the symmetric high-order network. Finally, a conclusion will be drawn in Section VI.

II. INTEGRATED SENSORLESS WIRELESS CHARGING SYSTEM

A. Integrated Wireless Charging in MCPs

Discrete wireless charging usually involves a two-stage lossy power conversion. To satisfy the charging requirements of millions of EVs, this two-stage power conversion can result in numerous negative impacts, such as more component counts, cost increase, efficiency reduction and environmental pollution. Therefore, integrated wireless charging is preferable by using a single-stage power conversion as depicted in Fig. 2. Generally, only one converter serves as an inverter or rectifier at the transmitter or receiver side, respectively. If a synchronous rectifier is used, the symmetric topologies including resonant networks and power converters can readily support the bidirectional integrated wireless charging. Meanwhile, either the modulation method or compensation network can help achieve both the CC and CV charging modes, thus no additional DC/DC converters. This integrated wireless charging can effectively improve the system cost-effectiveness and efficiency in the MCPs, thanks to experiencing less power conversion. For EV wireless charging in MCPs, wireless chargers should be targeted to meet the special requirements: 1) Robust system structure; 2) high energy density; 3) high reliability and low cost; 4) high fault tolerance; and 5) environmental friendliness and sustainability.

B. Symmetric Charging Network

To realize the CC and CV charging, the modulation method usually depends on the feedback of control parameters such as battery current and voltage. To solve this problem, the compensation network can be artfully designed to generate both the CC and CV outputs. Generally, the resonant network should meet the following three targets necessary for wireless charging: 1) ZPA operation, namely, input impedance angle is zero for unity power factor; 2) constant current gain $\mathbf{G}_{\mathrm{vi}}$ of the output current to the input voltage; and 3) constant voltage gain $\mathbf{G}_{\mathrm{vv}}$ of the output voltage to the input voltage. Hence, some typical low-order networks and high-order networks are analyzed in detail in the following parts.

a) Low-Order Network

In Fig. 3, four typical low-order networks are classified into two groups, namely the symmetric topology and asymmetric topology. The symmetric circuits can conveniently offer the symmetric input-output characteristics during the bidirectional charging operation. Thus, the symmetric topologies of series-series (SS) and parallel-parallel (PP) networks in Fig. 3(a) are analyzed mathematically in Table I, while the asymmetric network can be readily derived from high-order networks such as the symmetric inductor-capacitor (*LC*) compensated network in Table II. Wherein, X_{t1}, X_{t2}, X_{t3} and X_{t4} denote the impedances of capacitors or inductors at the transmitter side, while X_{r1}, X_{r2}, X_{r3} and X_{r4} denote those at the receiver side. Also, R is the load resistance; Z_r is the receiver's self-impedance; Z_{ref} is the reflected impedance; and Z_{in} is the transmitter's input impedance. Angular frequencies ω_{cc} and ω_{cv} are for the CC and CV modes, respectively, corresponding to two resonant frequencies f_{cc} and f_{cv}. Besides, $\Re(\cdot)$ denotes the real part, and $\Im(\cdot)$ denotes the imaginary part.

In Table I, the output current gain $\mathbf{G}_{vi}$, output voltage gain $\mathbf{G}_{vv}$ and ZPA operation are assessed. Accordingly, the SS topology can generate the load-independent CC and CV outputs by switching the operating frequencies. Nonetheless, the SS topology can succeed in achieving the ZPA operation in the CC mode but fails in the CV mode. Therefore, the reactive power of the inverter will increase significantly in the CV mode. On the other hand, the PP topology fails to work in the CC mode because the constraint conditions of $(\omega_{cc}M)^2=X_{t1}(X_{r1}+X_{r2})$ and $X_{t2}X_{r2}\neq0$ cannot be satisfied simultaneously. If the coupling coefficient could be nearly unity, it yields $(\omega_{cc}M)^2\simeq X_{t1}X_{r1}$, and thus the PP topology can operate in the quasi-CV mode. However, the PP topology will work at the non-ZPA operation in both the CC and CV modes.

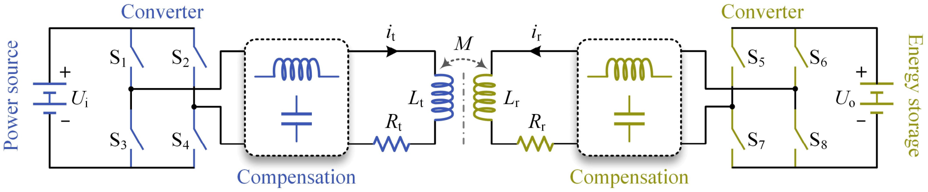

Fig. 2. Integrated wireless charging using a general compensation network.

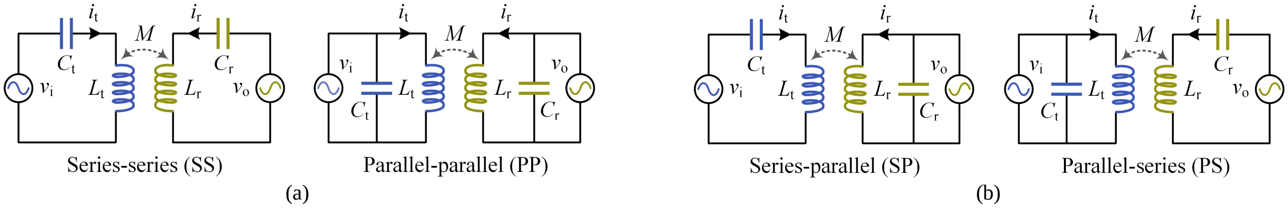

(a)

(b)

Fig. 3. Four basic compensation circuits. (a) Symmetric topology. (b) Asymmetric topology.

TABLE I

GENERAL ANALYSIS OF LOW-ORDER CIRCUIT TOPOLOGY

Circuit topology	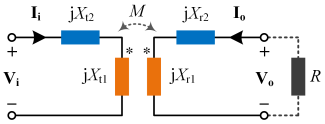	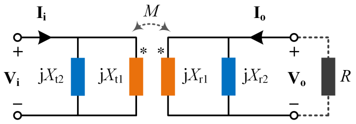
Output current gain $\mathbf{G}_{vi}=\dfrac{\mathbf{I}_o}{\mathbf{V}_i}$	$X_{t1}+X_{t2}=0\Rightarrow$ (CC mode at ω_{cc}) $\mathbf{G}_{vi}=\dfrac{j\omega_{cc}M}{j(X_{t1}+X_{t2})R+\left[(\omega_{cc}M)^2-(X_{t1}+X_{t2})(X_{r1}+X_{r2})\right]}=\dfrac{j}{\omega_{cc}M}$	$(\omega_{cc}M)^2\neq X_{t1}(X_{r1}+X_{r2}),\ X_{t2}X_{r2}\neq0\Rightarrow$ (Non-CC mode at ω_{cc}) $\mathbf{G}_{vi}=\dfrac{-j\omega_{cc}MX_{t2}X_{r2}}{(\omega_{cc}M)^2X_{t2}\left[jR-X_{r2}\right]-X_{t1}X_{t2}\left[j(X_{r1}+X_{r2})R-X_{r1}X_{r2}\right]}$
Output voltage gain $\mathbf{G}_{vv}=\dfrac{\mathbf{V}_o}{\mathbf{V}_i}$	$(\omega_{cv}M)^2=(X_{t1}+X_{t2})(X_{r1}+X_{r2}),\ X_{t1}+X_{t2}\neq0\Rightarrow$ (CV mode at ω_{cv}) $\mathbf{G}_{vv}=\dfrac{j\omega_{cv}MR}{j(X_{t1}+X_{t2})R+\left[(\omega_{cv}M)^2-(X_{t1}+X_{t2})(X_{r1}+X_{r2})\right]}=\dfrac{\omega_{cv}M}{X_{t1}+X_{t2}}$	$(\omega_{cv}M)^2\simeq X_{t1}X_{r1},\ X_{t2}X_{r2}\neq0\Rightarrow$ (Quasi-CV mode at ω_{cv}) $\mathbf{G}_{vv}=\dfrac{-j\omega_{cv}MX_{t2}X_{r2}R}{(\omega_{cv}M)^2X_{t2}\left[jR-X_{r2}\right]-X_{t1}X_{t2}\left[j(X_{r1}+X_{r2})R-X_{r1}X_{r2}\right]}$
ZPA operation $\varphi=\arctan\left(\dfrac{\Im(Z_{in})}{\Re(Z_{in})}\right)$	$Z_{in}=\dfrac{(\omega M)^2R}{R^2+(X_{r1}+X_{r2})^2}+j\left(X_{t1}+X_{t2}-\dfrac{(\omega M)^2(X_{r1}+X_{r2})}{R^2+(X_{r1}+X_{r2})^2}\right)$ $X_{t1}+X_{t2}=0,\ X_{r1}+X_{r2}=0\Rightarrow\Im(Z_{in})=0$ (ZPA in CC mode at ω_{cc}) $(\omega_{cv}M)^2=(X_{t1}+X_{t2})(X_{r1}+X_{r2}),\ X_{t1}+X_{t2}\neq0\Rightarrow\Im(Z_{in})\neq0$ (Non-ZPA in CV mode at ω_{cv})	$Z_r=\dfrac{X_{r2}^{\,2}R}{R^2+X_{r2}^{\,2}}+j\left(\dfrac{(X_{r1}+X_{r2})R^2+X_{r1}X_{r2}^{\,2}}{R^2+X_{r2}^{\,2}}\right)\Rightarrow\Im(Z_r)\neq0$ $Z_{in}=\dfrac{1}{\dfrac{1}{jX_{t2}}+\dfrac{Z_r}{jX_{t1}Z_r+(\omega M)^2}}\Rightarrow\Im(Z_{in})\neq0$ (Non-ZPA)

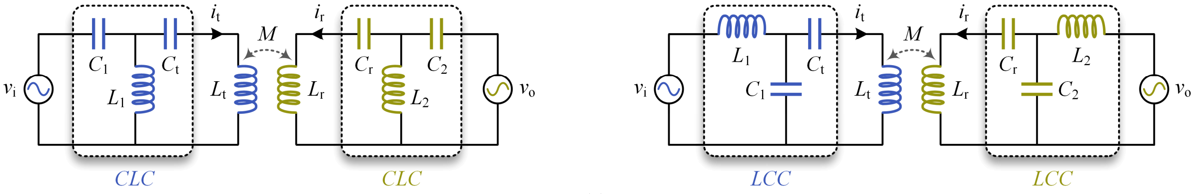

(a)

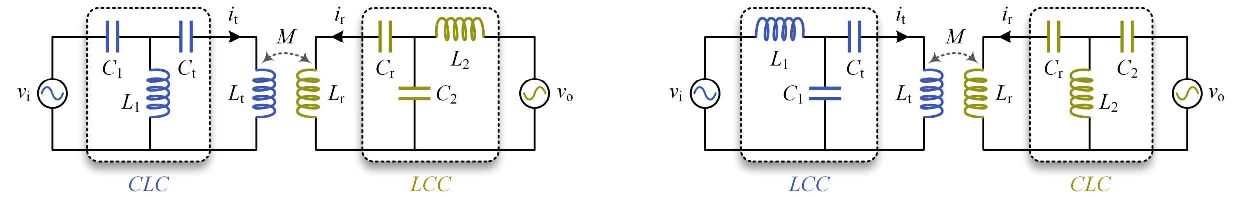

(b)

Fig. 4. High-order networks. (a) Symmetric topology. (b) Asymmetric topology.

TABLE II
GENERAL ANALYSIS OF HIGH-ORDER CIRCUIT TOPOLOGY

Circuit topology	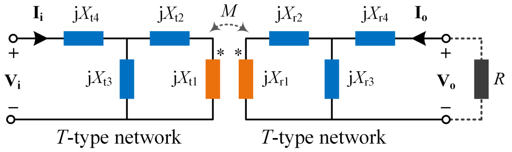
Output current gain $\mathbf{G_{vi}}=\dfrac{\mathbf{I_o}}{\mathbf{V_i}}$	$\mathbf{G_{vi}}=\dfrac{\overbrace{-\mathrm{j}\omega_{cc}MX_{t3}X_{r3}}^{X}}{\underbrace{(\omega_{cc}M)^2(X_{t3}+X_{t4})[\mathrm{j}R-(X_{r3}+X_{r4})]}_{Y_1}-\underbrace{[(X_{t1}+X_{t2})(X_{t3}+X_{t4})+X_{t3}X_{t4}]}_{Y_2}\underbrace{[\mathrm{j}(X_{r1}+X_{r2}+X_{r3})R-(X_{r1}+X_{r2})(X_{r3}+X_{r4})-X_{r3}X_{r4}]}_{Y_3}}$ $=\dfrac{X}{A+jB}\simeq C_{vi}\Rightarrow B\propto R,\quad A\gg B$ (CC mode at ω_{cc})
Output voltage gain $\mathbf{G_{vv}}=\dfrac{\mathbf{V_o}}{\mathbf{V_i}}$	$\mathbf{G_{vv}}=\dfrac{\overbrace{-\mathrm{j}\omega_{cv}MX_{t3}X_{r3}}^{X}R}{\underbrace{(\omega_{cv}M)^2(X_{t3}+X_{t4})[\mathrm{j}R-(X_{r3}+X_{r4})]}_{Y_1}-\underbrace{[(X_{t1}+X_{t2})(X_{t3}+X_{t4})+X_{t3}X_{t4}]}_{Y_2}\underbrace{[\mathrm{j}(X_{r1}+X_{r2}+X_{r3})R-(X_{r1}+X_{r2})(X_{r3}+X_{r4})-X_{r3}X_{r4}]}_{Y_3}}$ $=\dfrac{X}{\dfrac{A}{R}+j\dfrac{B}{R}}\simeq C_{vv}\Rightarrow\dfrac{A}{R}\propto R,\quad\dfrac{A}{R}\ll\dfrac{B}{R}$ (CV mode at ω_{cv})
ZPA operation $\varphi=\arctan\left(\dfrac{\Im(Z_{in})}{\Re(Z_{in})}\right)$	$Z_r=\dfrac{X_{r3}{}^2R}{R^2+(X_{r3}+X_{r4})^2}+\mathrm{j}\left(\dfrac{(X_{r1}+X_{r2}+X_{r3})R^2+X_{r3}X_{r4}(X_{r3}+X_{r4})+(X_{r1}+X_{r2})(X_{r3}+X_{r4})^2}{R^2+(X_{r3}+X_{r4})^2}\right),\ Z_{ref}=\dfrac{(\omega M)^2}{Z_r}$ $Z_{in}=\dfrac{X_{t3}{}^2Z_{ref}}{Z_{ref}{}^2+(X_{t1}+X_{t2}+X_{t3})^2}+\mathrm{j}\left(\dfrac{(X_{t3}+X_{t4})Z_{ref}{}^2+X_{t3}(X_{t1}+X_{t2})(X_{t1}+X_{t2}+X_{t3})+X_{t4}(X_{t1}+X_{t2}+X_{t3})^2}{Z_{ref}{}^2+(X_{t1}+X_{t2}+X_{t3})^2}\right)\Rightarrow\dfrac{\Im(Z_{in})}{\Re(Z_{in})}\simeq 0$ (ZPA in CC mode at ω_{cc} and CV mode at ω_{cv})
Circuit topology	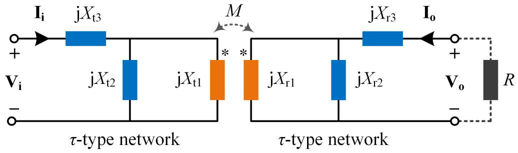
Output current gain $\mathbf{G_{vi}}=\dfrac{\mathbf{I_o}}{\mathbf{V_i}}$	$\mathbf{G_{vi}}=\dfrac{\overbrace{-\mathrm{j}\omega_{cc}MX_{t3}X_{r3}}^{X}}{\underbrace{(\omega_{cc}M)^2(X_{t2}+X_{t3})[\mathrm{j}R-(X_{r2}+X_{r3})]}_{Y_1}-\underbrace{[X_{t1}(X_{t2}+X_{t3})+X_{t2}X_{t3}]}_{Y_2}\underbrace{[\mathrm{j}(X_{r1}+X_{r2})R-X_{r1}(X_{r2}+X_{r3})-X_{r2}X_{r3}]}_{Y_3}}$ $=\dfrac{X}{A+jB}\simeq C_{vi}\Rightarrow B\propto R,\quad A\gg B$ (CC mode at ω_{cc})
Output voltage gain $\mathbf{G_{vv}}=\dfrac{\mathbf{V_o}}{\mathbf{V_i}}$	$\mathbf{G_{vv}}=\dfrac{\overbrace{-\mathrm{j}\omega_{cv}MX_{t3}X_{r3}}^{X}R}{\underbrace{(\omega_{cv}M)^2(X_{t2}+X_{t3})[\mathrm{j}R-(X_{r2}+X_{r3})]}_{Y_1}-\underbrace{[X_{t1}(X_{t2}+X_{t3})+X_{t2}X_{t3}]}_{Y_2}\underbrace{[\mathrm{j}(X_{r1}+X_{r2})R-X_{r1}(X_{r2}+X_{r3})-X_{r2}X_{r3}]}_{Y_3}}$ $=\dfrac{X}{\dfrac{A}{R}+j\dfrac{B}{R}}\simeq C_{vv}\Rightarrow\dfrac{A}{R}\propto R,\quad\dfrac{A}{R}\ll\dfrac{B}{R}$ (CV mode at ω_{cv})
ZPA operation $\varphi=\arctan\left(\dfrac{\Im(Z_{in})}{\Re(Z_{in})}\right)$	$Z_r=\dfrac{X_{r2}{}^2R}{R^2+(X_{r2}+X_{r3})^2}+\mathrm{j}\left(\dfrac{(X_{r1}+X_{r2})R^2+X_{r2}X_{r3}(X_{r2}+X_{r3})+X_{r1}(X_{r2}+X_{r3})^2}{R^2+(X_{r2}+X_{r3})^2}\right),\ Z_{ref}=\dfrac{(\omega M)^2}{Z_r}$ $Z_{in}=\dfrac{X_{t2}{}^2Z_{ref}}{Z_{ref}{}^2+(X_{t1}+X_{t2})^2}+\mathrm{j}\left(\dfrac{(X_{t2}+X_{t3})Z_{ref}{}^2+X_{t1}X_{t2}(X_{t1}+X_{t2})+X_{t3}(X_{t1}+X_{t2})^2}{Z_{ref}{}^2+(X_{t1}+X_{t2})^2}\right)\Rightarrow\dfrac{\Im(Z_{in})}{\Re(Z_{in})}\simeq 0,$ subject to $\begin{cases}\mathrm{j}X_{t2}=\mathrm{j}\omega L_{t2}+1/(\mathrm{j}\omega C_{t2})\\ \mathrm{j}X_{r3}=\mathrm{j}\omega L_{r3}+1/(\mathrm{j}\omega C_{r3})\end{cases}$ (ZPA in CC mode at ω_{cc} but non-ZPA in CV mode at ω_{cv} subject to X_{t2} and X_{r3} are single components, while ZPA in CV mode at ω_{cv} subject to X_{t2} and X_{r3} are *LC* in series, namely L_{t2} and C_{t2} as well as L_{r3} and C_{r3})

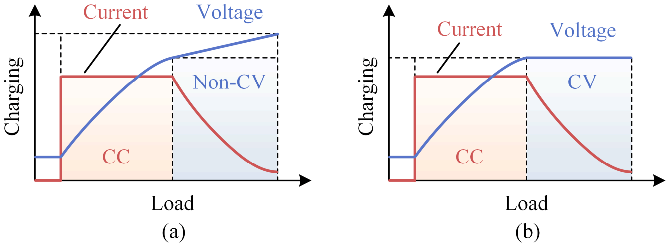

Fig. 5. Theoretical waveforms of CC and CV charging using symmetric topologies. (a) Single-frequency network. (b) Double-frequency network.

b) High-Order Network

In Fig. 4, four typical high-order networks are also classified into symmetric and asymmetric topologies. In particular, the symmetric topologies include the symmetric capacitor-inductor-capacitor (*CLC*) and *LCC* compensated networks in Fig. 4(a), which can offer the symmetric input-output characteristics for the peer-to-peer wireless charging. The output current gain $\mathbf{G}_{\mathbf{vi}}$, output voltage gain $\mathbf{G}_{\mathbf{vv}}$ and ZPA operation are evaluated mathematically in Table II.

The symmetric *T*-type compensation network can succeed in achieving the CC mode at ω_{cc} and the CV mode at ω_{cv} while maintaining the ZPA operation in both modes. In Table II, C_{vi} and C_{vv} are constant numbers. In the CC mode, the CC condition is that the imaginary part B is zero and much less than the real part A in the denominator of $\mathbf{G}_{\mathbf{vi}}$, namely $A>>B$. Wherein, B is related to R, while A is unrelated to R. Hence, $\mathbf{G}_{\mathbf{vi}}$ can be constant, thus enabling the load-independent CC output. In the CV mode, the CV condition is that the real part A/R is zero and much less than the imaginary part B/R in the denominator of $\mathbf{G}_{\mathbf{vv}}$, namely $A/R<<B/R$. Also, A/R is related to R, while B/R is unrelated to R, where B is proportional to R. Therefore, $\mathbf{G}_{\mathbf{vv}}$ can be constant, thus enabling the load-independent CV output. The design procedure reported in [15] is used to determine the parameters of the double-frequency *T*-type network. The numerical analysis method can model the WPT network and verify the theoretical analysis in Table II. Finally, $A>>B$ and $A/R<<B/R$ can be ensured to enable the load-independent CC and CV modes at two frequencies, respectively. In contrast, the symmetric τ-type compensation network can readily succeed in achieving the CC and CV modes as well as the ZPA operation in the CC mode. However, with the single-component X_{t2} and X_{r3}, the design of τ-type networks hits bottlenecks in maintaining the ZPA operation in both modes due to less design freedom. With the *LC*-series X_{t2} and X_{r3}, both the CC-ZPA and CV-ZPA can be achievable.

The high-order τ-type network can be simplified to analyze the low-order networks. For example, assuming $X_{t3}=0$ and $X_{r2}=\infty$, the parallel-series (PS) network can be generated and assessed. Assuming $X_{t2}=\infty$ and $X_{r3}=0$, the series-parallel (SP) network can be generated and assessed. As a result, both the PS and SP networks are hard to achieve the CC and CV modes with the ZPA operation simultaneously while observing the frequency standard of 81.39 kHz~90.0 kHz specified in SAE J2954. These low-order networks suffer from less design freedom. The low-order SS topology cannot achieve the inherent ZPA operation in the CV mode, while the low-order SP topology can achieve neither CC nor CV mode and fails to realize ZPA operation, which cause various disadvantages, such as reduced system efficiency, challenging heat dissipation, and increased system cost and volume. The high-order *LCC-LCC* topology can inherently achieve both CC and CV modes while maintaining ZPA operation, which is highly desired by the wireless charging of electric vehicles. Hence, the *LCC-LCC* topology is chosen as an exemplification in this paper.

c) Symmetric LCC Network

In single-frequency network design, the symmetric *LCC* network can readily achieve either the CC or CV mode, which depends on the use of a CV or CC source. Generally, the voltage-source inverter is usually used to energize the WPT network. Suffering from the inherent system characteristics, the single-frequency network can enable either CC or CV mode only, unless additional power control with pulse modulation or input voltage regulation by an additional DC-DC converter is employed. Hence, the CC charging can be inherently activated to make the charging current stabilize with constancy and impervious to the load changes, while the CV charging cannot be maintained because the charging voltage grows and the charging current drops continuously with the load increase, as shown in Fig. 5(a). To enable one fixed network with both the CC and CV modes in Fig. 5(b), the symmetric *LCC* network should be configured as a double-frequency network. It aims to meet the following four goals: 1) Two resonant frequencies (f_{cc} and f_{cv}) are subject to the EV wireless charging standard such as SAE J2954; 2) one resonant frequency f_{cc} is in charge of the CC mode, and the other f_{cv} is in charge of the CV mode; 3) both the CC and CV modes should maintain the ZPA operation with load changes; and 4) both modes should be high-efficiency.

III. SYSTEM SUPERIORITY AND INSENSITIVITY

A. Integrated Sensorless Wireless Charger

In Fig. 6, the proposed integrated SWC system uses a symmetric *LCC* network to achieve the CC and CV charging with the ZPA operation. The whole system including the resonant networks and converter topologies is symmetric between the transmitter and receiver sides. Wherein, U_i, I_i, v_i, i_i and i_t are the DC input voltage, DC input current, AC input voltage, AC input current and transmitter resonant current, respectively. Symmetrically, U_o, I_o, v_o, i_o and i_r are the DC output voltage, DC output current, AC output voltage, AC output current and receiver resonant current, respectively. Inductor L_1, capacitor C_1 and capacitor C_t form the primary *LCC* compensation network, while L_2, C_2 and C_r form the secondary *LCC* compensation network. Besides, the gallium nitride (GaN) H-bridge inverter is populated with four switches S_1–S_4, while the H-bridge rectifier is populated with four diodes D_1–D_4. For bidirectional charging, a synchronous rectifier can be used to replace the diode rectifier by deploying active switches, thus having symmetric converters.

Conventional wireless chargers rely on feedback sensors and communication modules for battery charging control. These chargers will malfunction once the sensors or communication modules are faulty. Differing from the conventional wireless chargers, the proposed integrated SWC does not require the sensors of charging voltage and current as well as communication modules. Significantly, the proposed charger can reliably switch between the CC and CV modes by sensing the transmitter input current only, without using additional DC/DC converters. The operating frequency and thus the charging modes will be switched once the threshold current is detected. Therefore, the proposed integrated SWC system has the advantages of onboard sensor-free, communication-free, high reliability, high compactness and high efficiency over its conventional counterparts.

The modulation strategy such as phase shift control (PSC) is optional and programmable. The use of modulation is to improve the applicability of the hardware charger to different battery packs. For example, the proposed charger can flexibly change the duty ratio in the modulation strategy without modifying the hardware components when charging for different battery packs such as different rated voltages or different equivalent internal resistances. Accordingly, the nth harmonic of input voltage v_i can be expressed as [11]:

$$v_{i,n}=\frac{4U_i}{n\pi}\sin(n\pi d)\cos\left(\frac{n\theta}{2}\right)\sin(n\omega t) \tag{1}$$

where d is the duty ratio usually at 50%, and θ is the shifted phase angle. The root-mean-square value of the fundamental component is $V_{i,1}=2\sqrt{2}\,U_i/\pi$. If $d<50\%$, the even-order harmonics can be generated apart from the odd-order harmonics.

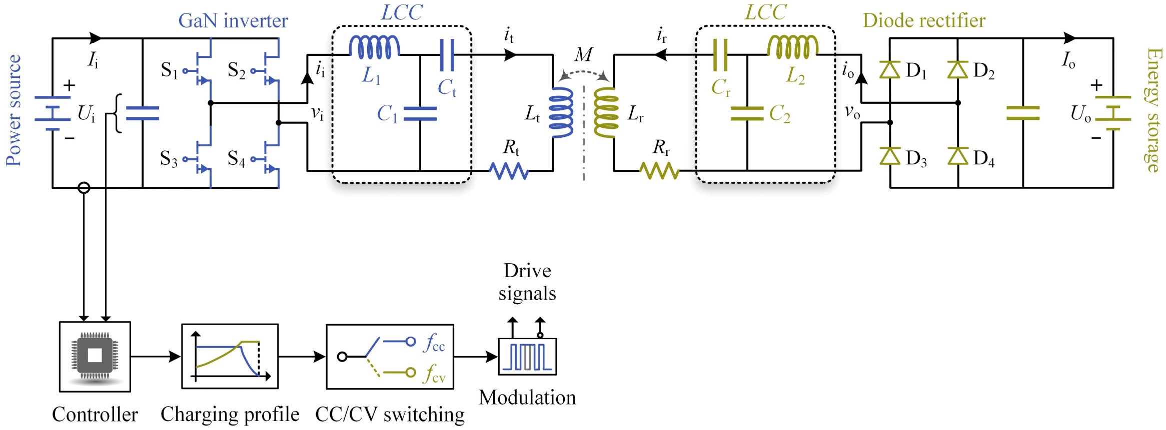

Fig. 6. Proposed integrated SWC system using a symmetric high-order network.

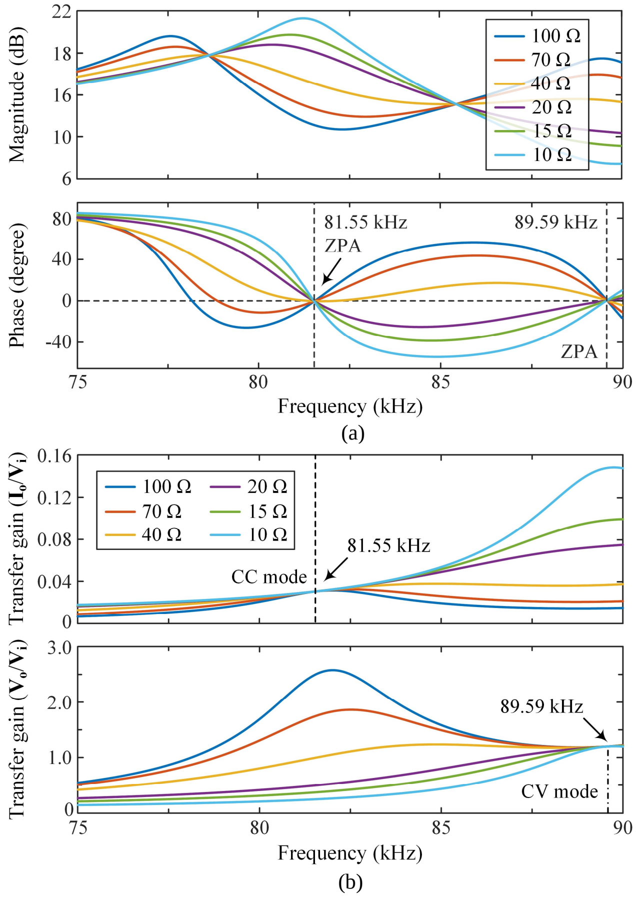

Fig. 7. Characteristics of symmetric high-order network. (a) Input impedance characteristics. (b) Load-independent transfer gains.

B. Superiority of Symmetry

Thanks to their good effectiveness and practicality, the wireless chargers are on target for three requirements: 1) CC and CV charging; 2) load-independent charging; and 3) high-efficiency charging, such as achieving ZPA operation or zero voltage switching. In the proposed integrated SWC, the use of the symmetric *LCC* network and converter topology offers some definite superiorities including the load-independent CC and CV charging, ZPA operation, reliable sensorless control without onboard feedbacks, and easy extension for bidirectional charging. Thus, it outperforms those single-frequency wireless chargers.

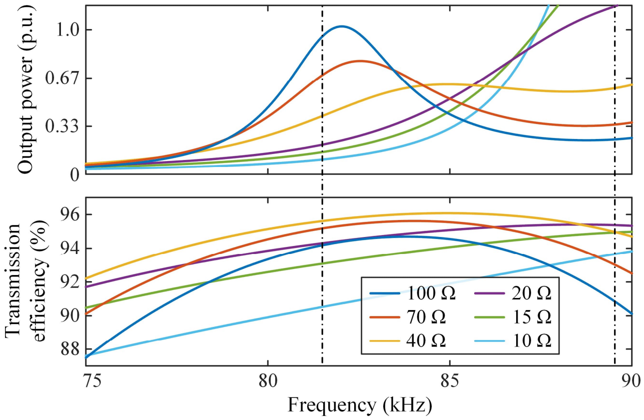

Fig. 8. Output powers and transmission efficiencies of proposed integrated SWC system using a symmetric network.

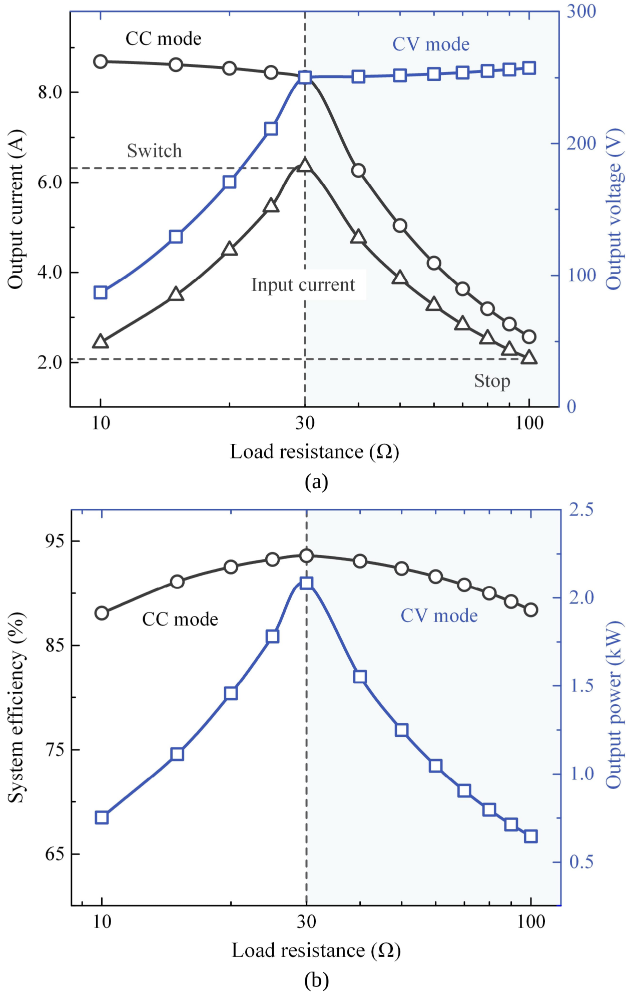

(a)

(b)

Fig. 9. Simulated system performance of proposed integrated SWC system. (a) Input-output characteristics during CC and CV charging modes. (b) System efficiency and output power.

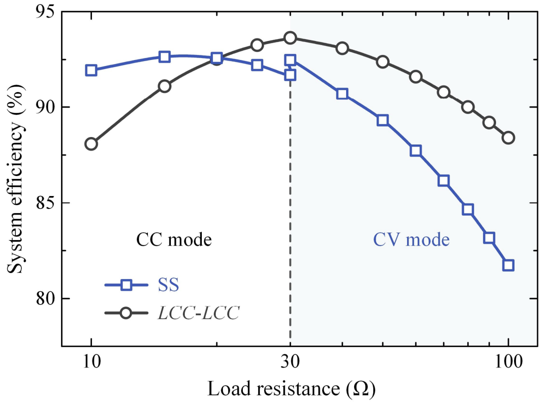

Fig. 10. System efficiency of wireless charging using double-frequency SS topology and proposed *LCC-LCC* topology.

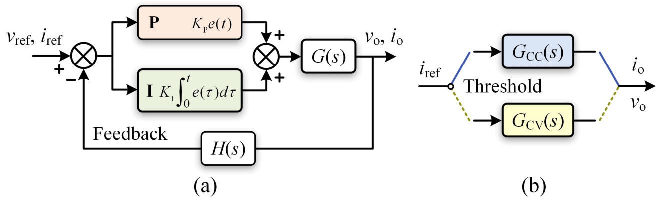

(a)

(b)

Fig. 11. Wireless charging control. (a) Sensor-based. (b) Sensorless.

To evaluate the superiorities, the characteristics of the symmetric high-order network are investigated in Fig. 7. In Fig. 7(a), the ZPA operation can be realized at two resonant frequencies of 81.55 kHz and 89.59 kHz with respect to different loads ranging from 10 Ω to 100 Ω. Fig. 7(b) shows the current transfer gain ($\mathbf{I}_{\mathbf{o}}/\mathbf{V}_{\mathbf{i}}$) and voltage transfer gain ($\mathbf{V}_{\mathbf{o}}/\mathbf{V}_{\mathbf{i}}$). Both gains can be kept constant at two operating frequencies for the CC and CV charging modes, respectively. These phenomena indicate that the CC and CV charging modes can be maintained and switched by operating at the above two frequencies. Besides, Fig. 8 shows the output power and transmission efficiency of the proposed integrated SWC system using a symmetric *LCC* network under different loads. At two resonant frequencies of 81.55 kHz and 89.59 kHz, the transmission efficiency can be always maintained over 90.5% and 90.8%, and their peak values can reach up to 95.6% and 95.4%, respectively.

C. Analyses of Performance and Sensitivity

To analyze the system performance, Fig. 9 shows the input-output characteristics, system efficiency and output power of the proposed integrated SWC system. Wherein, a switching point of 30-Ω load is selected as an exemplification. The determination of a switching point between the CC and CV modes is based on the battery equivalent load. Batteries having different specifications will exhibit different switching points. Instead of hardware re-design, software adjustment of PSC can be readily applied to make the hardware system suitable for different specifications of batteries. It has the advantages of high convenience, high applicability, high cost-effectiveness and time-saving. The equivalent series resistances of polypropylene film capacitors are accounted for in assessing the system efficiency.

In Fig. 9(a), the proposed wireless charger can successfully achieve the CC and CV charging modes under a varying load resistance. It can be observed that the CC mode has an insignificant deviation in charging current by only ±2.1%, while the CV mode has an insignificant deviation in charging voltage by only ±1.4%, which are totally acceptable for battery charging. Besides, the maximum value of transmitter input current occurs at the transition from the CC mode to CV mode. Thus, detecting the maximum input current as a threshold can readily determine the switching point between the CC and CV modes. With the use of only a current sensor at the transmitter side, there is no need to involve any onboard feedback for charging management. Fig. 9(b) shows the simulated system efficiency and output power with respect to different loads. Wherein, the maximum system efficiency can reach 93.6%, and the output power reaches its maximum value at the transition point of charging modes. Meanwhile, the system efficiency can be maintained always higher than 88.1% even at a light load. With 5% parameter variations of inductors L_1 and L_2, the effects on outputs are insignificant in the CC and CV modes. Moreover, the output errors caused by parameter variations can be suppressed effectively by improving the parameter precision of capacitors C_{t}, C_{r}, C_1 and C_2 or applying online parameter identification and correction.

Fig. 10 shows the system efficiency of different topologies. The SS topology has slightly higher energy efficiency than the proposed *LCC-LCC* topology considering the whole CC mode. The peak efficiency of the SS topology is slightly lower, which is due to 1) the high DC voltage required for outputting a rated active power in the non-ZPA CV mode, 2) hard switching operation in the CC mode, and 3) specified working conditions of loads. In the CV mode, however, the SS topology has greatly lower efficiency, which is due to the non-ZPA operation and the need to handle large reactive power by hard switching in the CV mode.

IV. SECONDARY SENSORLESS CHARGING CONTROL

A. Sensor-Based Charging Control

By using the technologies of wireless communication such as Bluetooth or simultaneous wireless power and data transfer, the conventional wireless charging control is usually based on the sensors to generate the feedback signals of onboard battery charging current i_o and voltage v_o. As an exemplification, Fig. 11(a) shows the typical block diagram of wireless sensor-based charging using a proportional-integral (PI) controller. Accordingly, the controller outputs can be calculated as:

$$\begin{cases} u_{CC}(t) = K_{P1}\left(i_{ref} - i_o\right) + K_{I1}\int_0^t \left(i_{ref} - i_o\right) d\tau \\ u_{CV}(t) = K_{P2}\left(v_{ref} - v_o\right) + K_{I2}\int_0^t \left(v_{ref} - v_o\right) d\tau \end{cases} \tag{2}$$

where K_{P1} and K_{P2} are the proportional gains; K_{I1} and K_{I2} are the integral gains; τ is the variable of integration; and v_{ref} and i_{ref} are the reference voltage and current, respectively; and $u_{CC}(t)$ and $u_{CV}(t)$ are the output voltages of transmitter inverter in the CC and CV modes, respectively.

However, this sensor-based wireless charging is challenged by two technical bottlenecks: 1) Significant delay in real-time communication [16] reduces the control stability and response speed; and 2) over-dependence on sensors and communication results in system disruptions once components malfunction.

B. Sensorless Charging Control

In the proposed symmetric SWC, the relationship between the AC input and AC output can be expressed as:

$$\begin{cases} \overline{v}_i i_i = v_o \overline{i}_o / \eta_{trans} \;\Rightarrow\; i_i = \mathbf{G_{vi}}(\omega_{cc}) v_o / \eta_{trans} \\ \overline{v}_i i_i = \overline{v}_o i_o / \eta_{trans} \;\Rightarrow\; i_i = \mathbf{G_{vv}}(\omega_{cv}) i_o / \eta_{trans} \end{cases} \tag{3}$$

where $\eta_{trans} \simeq 1$ is the transmission efficiency. The transmitter is powered by a constant and controllable voltage source with a root-mean-square value of $V_i = 2\sqrt{2}\cos(\theta/2)U_i/\pi$. During the CC mode, both the input voltage $\overline{v}_i$ and charging current $\overline{i}_o$ are constant. The charging voltage v_o increases gradually with the increasing load, and thus the input current i_i increases. Also, the input current i_i is linearly correlated to the charging voltage v_o. During the CV mode, both $\overline{v}_i$ and $\overline{v}_o$ are constant, and both i_i and i_o decrease gradually with the decreasing load. Also, i_i is linearly correlated to i_o. Therefore, control of i_i at the transmitter side can manage v_o and i_o at the receiver side without using onboard sensors and communication modules. Threshold detection of the input current i_i can decide to switch the frequencies and thus change the charging modes. Fig. 11(b) shows the block diagram of the proposed SWC system.

The DC input-output relationship can be calculated as:

$$\begin{cases} \overline{U}_i I_i = U_o \overline{I}_o / \eta_{sys} \;\Rightarrow\; I_i \simeq \mathbf{G_{vi}}(\omega_{cc}) U_o / \eta_{sys} \quad \text{(CC mode)} \\ \overline{U}_i I_i = U_o \overline{I}_o / \eta_{sys} \;\Rightarrow\; I_i \simeq \mathbf{G_{vv}}(\omega_{cv}) I_o / \eta_{sys} \quad \text{(CV mode)} \end{cases} \tag{4}$$

where η_{sys} is the system efficiency. Finally, sensing the DC input current I_i only can also determine the transition point of switching between the CC and CV modes, thus managing the proposed symmetric SWC system effectively. With the help of the proposed symmetric network, the PSC can regulate the current, voltage and power level during the CC and CV modes.

TABLE III
DESIGN SPECIFICATIONS AND PARAMETERS OF PROTOTYPE

	Parameter	Value/type
	DC input voltage (U_i)	350 V
Transmitter	Coil turn (n_t)	10
	Coil inductance (L_t)	106.4 μH
	Coil internal resistance (R_t)	0.09 Ω
	Matched capacitance (C_t)	47.6 nF
	Filter inductance (L_1)	47.0 μH
	Filter internal resistance (R_1)	0.02 Ω
	Filter capacitance (C_1)	133.0 nF
Receiver	Coil turn (n_r)	10
	Coil inductance (L_r)	104.6 μH
	Coil internal resistance (R_r)	0.07 Ω
	Matched capacitance (C_r)	49.0 nF
	Filter inductance (L_2)	42.5 μH
	Filter internal resistance (R_2)	0.01 Ω
	Filter capacitance (C_2)	120.0 nF
	Transfer distance (D_p)	150 mm
	Mutual inductance (M)	15.1 μH
	Nominal resonant frequencies (f_{cc}, f_{cv})	81.55, 89.59 kHz
	GaN inverter (two half-bridges)	GSP65R13HB
	Digital signal processor (DSP)	TMS320F28335

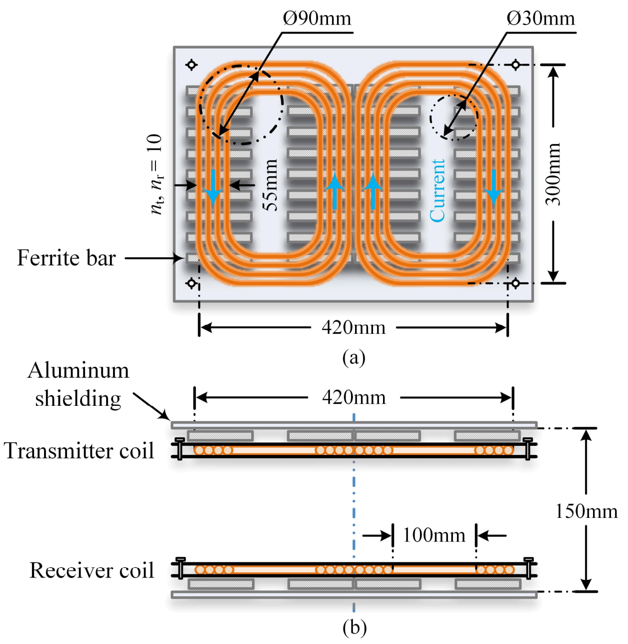

Fig. 12. Geometries of coils. (a) Transmitter or receiver. (b) Displacement.

V. RESULTS AND VERIFICATIONS

To verify the feasibility of the proposed integrated SWC system, both the finite element analysis (FEA) simulation and hardware experimentation are performed. The design specifications and parameters are listed in Table III. All waveforms are recorded by an oscilloscope (LeCroy 6100A) with the current and voltage probes (CP030 and ADP300). All powers and efficiencies are measured by a precision power analyzer (YOKOGAWA WT3000). The power load is realized by using two electronic loads (PLZ2005WH2) in parallel. The GaN inverter is populated with GaN transistors of GS66516B, while the rectifier adopts power diodes of BYV34-400. Detailed geometries with dimensions of charging coils are depicted in Fig. 12, where the transmitter and receiver adopt the same double-D coils. Ferrite bars are used to enhance the mutual inductance. Aluminum plates are to perform the magnetic shielding. To wind coils, the specification of Litz wires is 1200×0.10 mm.

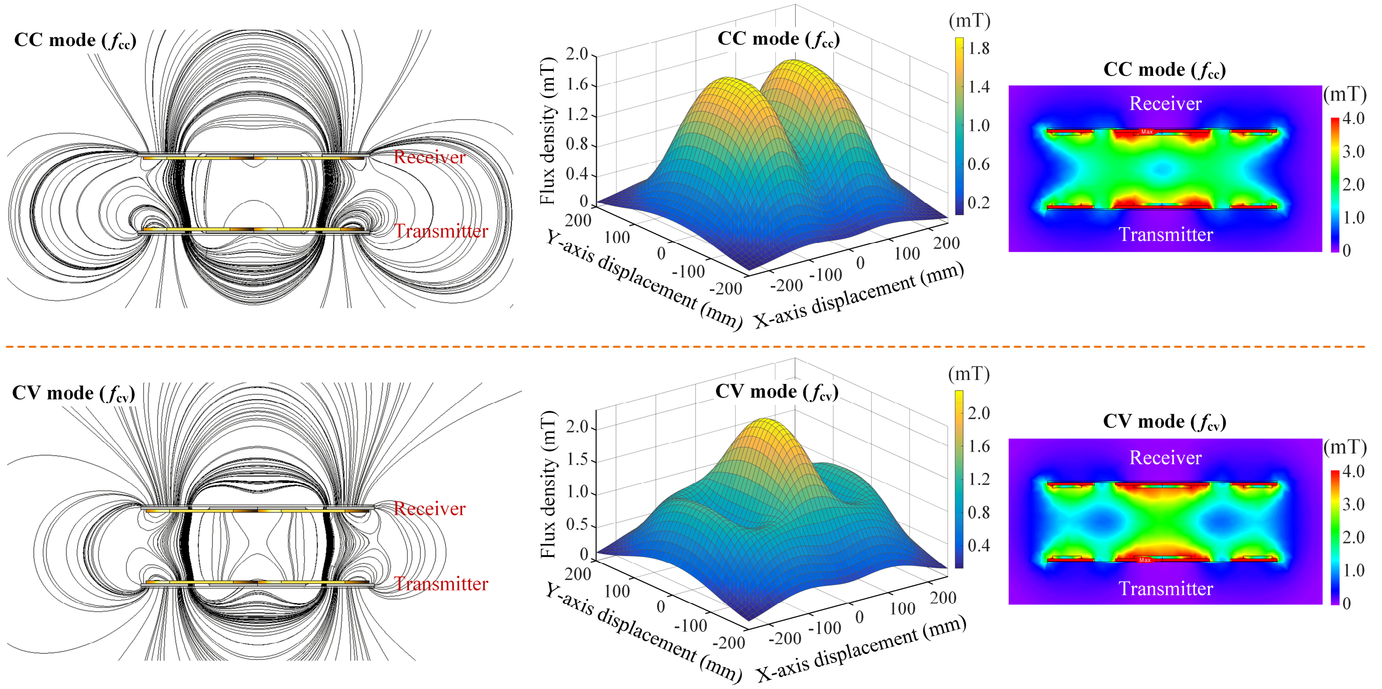

(a) (b) (c)

Fig. 13. FEA of electromagnetic field patterns. (a) Flux lines. (b) 3-D flux densities along middle parallel plane. (c) 2-D flux densities along middle vertical plane.

A. Simulation Results

To assess the electromagnetic characteristics of the proposed integrated SWC system, an FEA model is built to calculate the electromagnetic field patterns in the CC and CV modes, respectively. Wherein, the DC voltage source is set as 350 V, and the equivalent AC load is 26.5 Ω. Due to the inevitable parameter errors, the double-frequency symmetric *LCC* network for FEA simulation is tuned at 80.03 kHz (CC mode) and 89.35 kHz (CV mode) which are slightly deviated from the frequencies in experimental verification. Whereas, it is still acceptable and effective for simulation verification by using the FEA method.

Magnetic shielding and human safety from electromagnetic exposure are very crucial for wireless charging. To provide better visualization, Fig. 13 shows the FEA results of electromagnetic field patterns, which is mainly to verify the effectiveness of the magnetic shielding designed for the proposed SWC system. In addition, the magnitudes of electromagnetic fields are nearly the same, which indicates not overly large current in the CC and CV modes. The reason why two peaks of electromagnetic fields in the CC mode while only one peak in CV mode is mainly the differences of current amplitudes between the transmitter and receiver coils. Firstly, Fig. 13(a) shows the magnetic flux lines circling through the transmitter and receiver double-D coils in the CC (top) and CV (bottom) modes. It can be observed that almost all flux lines walk through the transmitter and receiver coils, and nearly no flux lines are dispersed. Secondly, Fig. 13(b) shows the three-dimensional (3-D) flux densities along the middle parallel plane between the transmitter and receiver coils in the above two modes. Wherein, the maximum flux densities can reach 1.911 mT in the CC mode and 2.275 mT in the CV mode. The difference of peak field patterns is due to the use of different frequencies for the CC and CV modes. The impedances and currents of transmitter and receiver differ between two modes. Thirdly, Fig. 13(c) shows the two-dimensional (2-D) flux densities along the middle vertical plane—a cutting plane of both the transmitter and receiver coils. It can be observed that the flux densities in the vicinity of WPT coils are much higher than those in other areas. Owing to magnetic shielding, flux densities inside the air gap between the WPT coils are much higher than those outside the air gap. These FEA results can be well visualized for assessing the magnetic performance and optimizing the system design. Finally, all these FEA results confirm that the proposed integrated SWC system can successfully achieve the CC and CV charging that is controlled by switching the frequencies.

B. Experimental Results

A proof-of-concept prototype is built for experimental demonstration as shown in Fig. 14. In experimentation, the CC mode operates at 81.55 kHz with a shifted phase angle of θ=0°, while the CV mode works at 89.59 kHz with a shifted phase angle of θ=99.4°. With different load resistances, Fig. 15 shows the measured waveforms of the proposed integrated SWC system, including the AC input voltage v_i and current i_i, DC output voltage U_o and current I_o, transmitter current i_t, and receiver current i_r. It can be observed from Fig. 15(a)–(c) that the charging current i_o keeps constant against the load changes from 15 Ω to 30 Ω in the CC mode. During the CC mode, zero voltage switching can be realized and maintained for suppressing the switching loss. In the CV mode, the phase shift of θ=99.4° is exemplified to ensure a smooth transition from the CC mode to CV mode. To adapt to charging for different types of batteries, the phase shift θ can be changed flexibly in the modulation strategy, instead of the need of hardware modification. It can also be observed from Fig. 15(d)–(f) that the charging voltage U_o maintains constant against the load variations from 30 Ω to 60 Ω in the CV mode. Therefore, these measured waveforms well confirm the load-independent input-output characteristics of CC and CV modes.

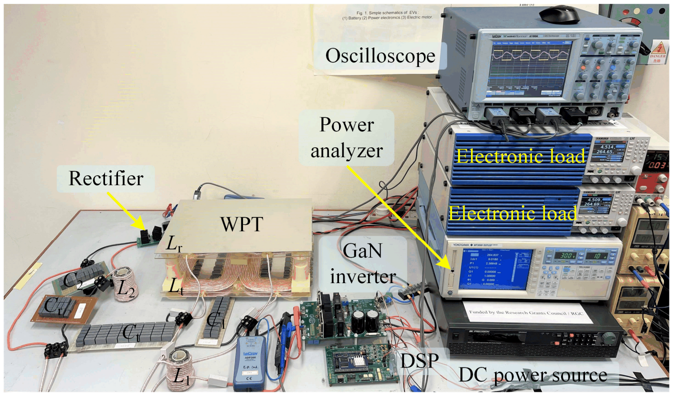

Fig. 14. Proof-of-concept prototype.

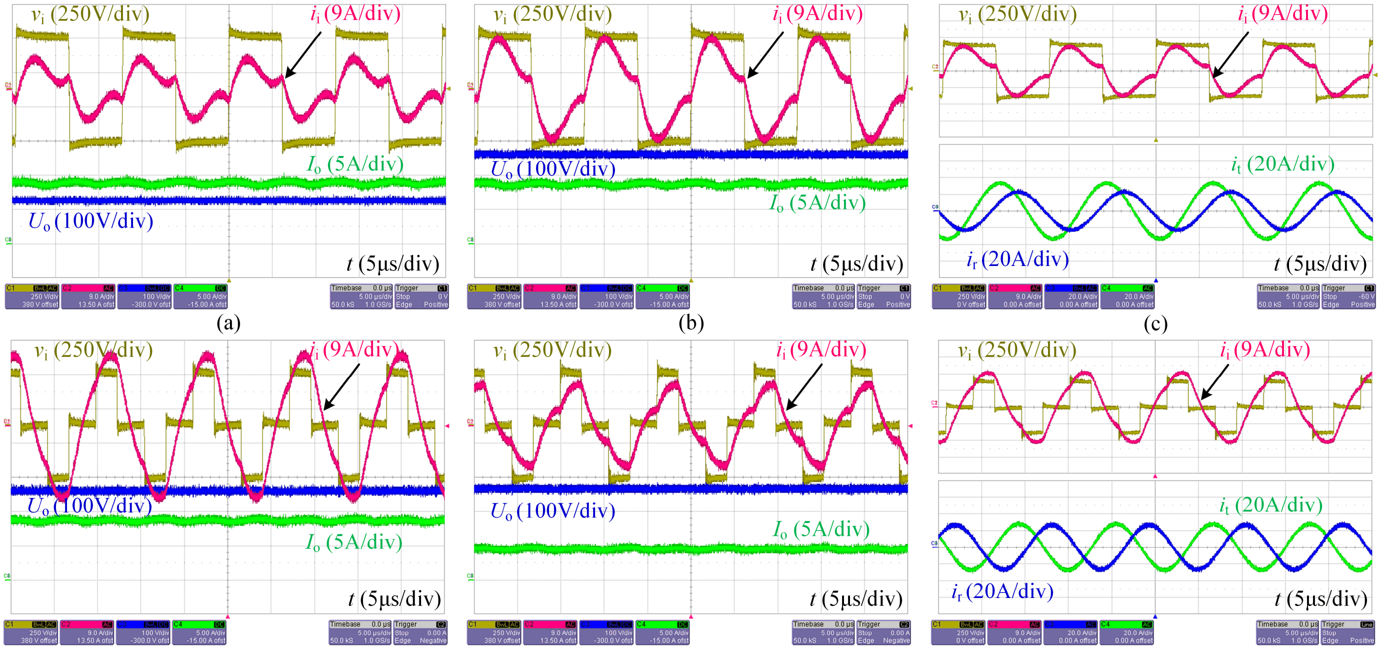

(a) (b) (c)

(d) (e) (f)

Fig. 15. Measured waveforms of proposed integrated SWC system. (a) CC mode at 15-Ω load. (b) CC mode at 30-Ω load. (c) Input-output characteristics in CC mode. (d) CV mode at 30-Ω load. (e) CV mode at 60-Ω load. (f) Input-output characteristics in CV mode.

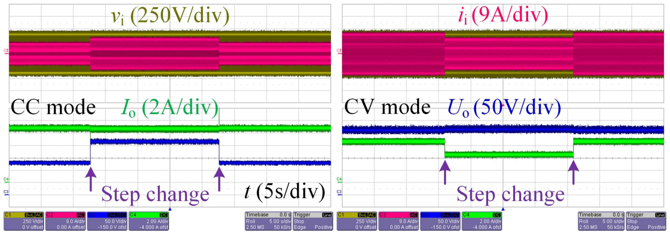

(a) (b)

Fig. 16. Dynamic responses to load step changes. (a) CC mode. (b) CV mode.

Furthermore, Fig. 16 shows the dynamic responses of the proposed integrated SWC system to the step changes of load resistance. In the CC mode, Fig. 16(a) shows the measured waveforms of AC input voltage v_i and current i_i as well as DC output voltage U_o and current I_o when the load experiences a step increase from 15 Ω to 25 Ω and then a step decrease from 25 Ω to 15 Ω. Correspondingly, the charging power increases from 1.16 kW to 1.90 kW and then decreases to 1.16 kW. Significantly, the charging current stabilizes with constancy in the CC mode, which is impervious to the step changes of load resistance. In the CV mode, Fig. 16(b) shows the measured waveforms during the dynamic responses when the load suddenly increases from 40 Ω to 60 Ω and then decreases from 60 Ω to 40 Ω. Correspondingly, the charging power decreases from 1.74 kW to 1.22 kW and then increases to 1.74 kW. Significantly, the charging voltage stabilizes with constancy in the CV mode, which is also impervious to the step changes of load resistance. Besides, the whole-process charging profile is measured as shown in Fig. 17, where the whole process of the highly autonomous SWC is accelerated to complete within around 160 s. The charging modes will be changed automatically by switching the operating frequencies once the DC input current I_i is detected to reach the peak value of 7.2 A. After entering the CV mode, the wireless charging process will be ended automatically once the DC input current I_i is detected to reach the valley value of 2.5 A, thus preventing battery overcharge. All these results confirm that the proposed integrated SWC system can successfully achieve the whole-process battery charging by automatic detection and management at the transmitter side only.

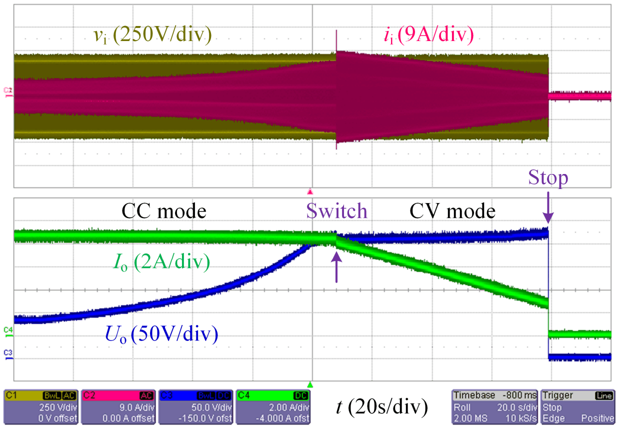

Fig. 17. Measured waveforms of integrated SWC process.

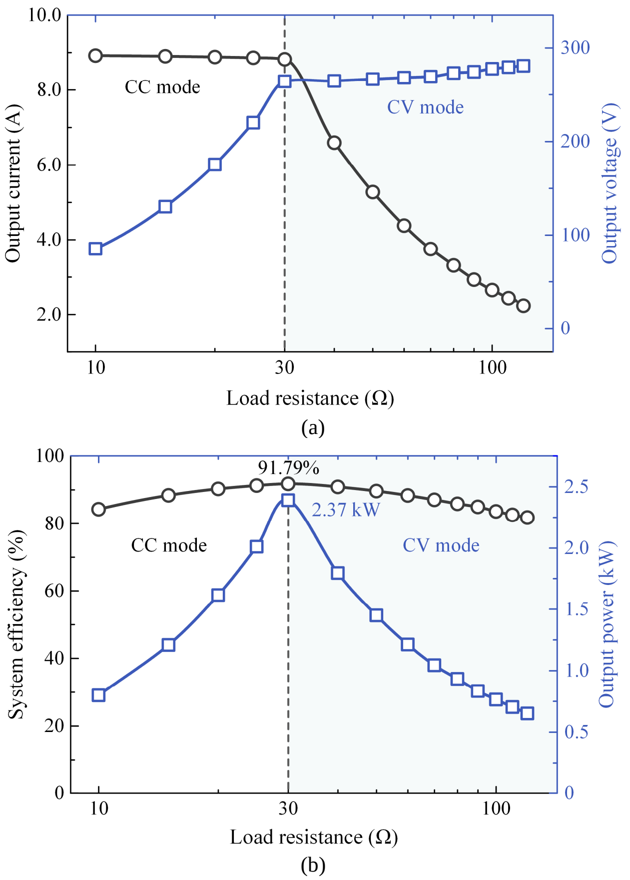

Fig. 18. Measured characteristics of proposed integrated SWC system. (a) CC and CV charging modes. (b) DC-to-DC system efficiency and output power.

Finally, to evaluate the system performance of proposed integrated SWC comprehensively, the output current I_o and output voltage U_o are measured with respect to the load resistance ranging from 10 Ω to 120 Ω, as shown in Fig. 18(a). It can be observed that the output current maintains constant at around 8.90 A with an insignificant decrease in the CC mode, while the output voltage maintains constant at around 275 V with an insignificant increase in the CV mode. The proposed SWC system can automatically end the charging process to protect the battery from overcharging. Furthermore, the DC-to-DC system efficiency and output power are measured based on the proposed integrated SWC system, as shown in Fig. 18(b). The maximum output power can reach up to 2.4 kW and happen at the transition point from the CC mode to CV mode. The DC-to-DC system efficiency can reach 91.8% at the charging power of 2.4 kW with a transfer distance of 150 mm. All these measured system performances well confirm that the proposed integrated SWC system can achieve the desired CC and CV battery charging while possessing the advantages of onboard sensor-free, communication-free, high efficiency and high reliability over its counterparts.

C. Discussion and Recommendation

Apart from the merits of sensorless charging control, the double-frequency network design can achieve comparable transmission efficiency and system efficiency to the single-frequency network design. Significantly, in addition to maximizing the peak efficiency, the whole-process energy efficiency [33] deserves more concern and improvement for the entire charging process. The proposed scheme can be applied in plenty of applications [33] including sensorless wireless charging for electric vehicles [34], portable devices [35], medical implants and robots [36]. This scheme can not only reduce the control complexity but potentially improve the system compactness and cost-effectiveness by eliminating the onboard sensors, controllers, communication modules and power converters. The novelty and new contributions of this paper can be summarized as follows:

1) In the MCPs, an integrated SWC scheme is proposed for EV wireless charging, which brings numerous advantages such as controller-free, sensor-free, communication-free, converter-free, and switch-free. Its low system cost, small space occupation, reduced system complexity, and high robustness are highly desirable for urban buildings.
2) General analyses of low-/high-order networks are comprehensively performed in the double-frequency design. By designing a double-frequency symmetric network, the load-independent CC and CV outputs can be inherently generated to enable the proposed SWC in the MCPs.
3) This integrated SWC scheme can conduct the autonomous management of CC and CV charging profile by detecting the current threshold to switch two resonant frequencies. It not only maintains ZPA operation but reduces the control complexity and improves the system reliability, which is preferable in the MCPs.
4) To charge different EVs in MCPs, this SWC system can be readily refitted by using software control rather than hardware modification, hence significantly improving the charging compatibility.
5) By reducing the use of electrical and electronic components, the proposed scheme has the merits of

environmental friendliness, cost-effectiveness, cost reduction and system compactness, hence promoting low carbon footprint and green-tech revolution.

A comprehensive comparison is given in Table IV. Significantly, the energy efficiency of the whole charging process, rather than peak efficiency or segment efficiency, should be considered comprehensively. The double-frequency *LCC-LCC* topology has numerous advantages of robust system structure, low control complexity, good fault tolerance and low cost while maintaining high efficiency during the whole charging process. The design of wireless charging coupler has considered the practical requirements, which can be applicable for field testing of EV wireless charging in MCPs. The proposed double-frequency *LCC-LCC* system takes the advantages of higher design freedom, higher system robustness and stability, lower control complexity, lower cost, and better environmental friendliness and sustainability over the three-coil WPT system [37].

To deal with the misalignment, an online detection unit of mutual inductance deserves to be developed in further efforts. Thus, the transmitter can be controlled to generate the desired outputs. Another approach to avoiding misalignment is to use the automated valet parking (AVP) technology. With the booming development of artificial intelligence and self-driving, the AVP technology can perfectly collaborate with the proposed wireless sensorless charging system by eliminating the misalignment, thus guaranteeing the output precision in the MCPs. Further efforts can be made to develop the AVP technology, aiming for fully automatic wireless charging while bringing charging convenience and high performance. Besides, transmitter-end battery fault diagnosis and intelligent observation of battery states including state of charge and state of temperature deserve to be developed in-depth to predict possible faults and real-time battery states.

TABLE IV
COMPREHENSIVE COMPARISON OF WIRELESS CHARGING TOPOLOGIES

Topology	Efficiency	Inherent CC/CV mode	ZPA	Robustness	Sensor and microcontroller	Cost
Single-frequency SS	High	CC: Yes CV: No	Yes	Low	Yes	High
Double-frequency SS	CC: High CV: Low	Yes	CC: Yes CV: No	Low	No	Low
Double-frequency *LCC-LCC*	High	Yes	Yes	High	No	Low

VI. CONCLUSION

In this paper, an integrated SWC system has been proposed and then implemented for EV wireless charging in the MCPs. This integrated SWC can thoroughly get rid of the dependence on sensing and communicating the receiver’s and battery’s states. It owns the definite merits of onboard sensor-free, communication-free, controller-free, converter-free and switch-free, thus embracing the environmental friendliness and carbon neutrality. With the help of a symmetric high-order network that enables the CC and CV charging with the ZPA operation inherently, threshold detection of the transmitter input current only can determine the transition point of switching the operating frequencies and thus changing the charging modes, finally managing the proposed integrated SWC system successfully. The DC-to-DC system efficiency can reach 91.8% based on a 2.4-kW proof-of-concept prototype at a 150-mm transfer distance. Both the software simulation and hardware experimentation are performed to verify the feasibility of proposed integrated SWC system using the symmetric high-order network.

REFERENCES

[1] G. A. Covic and J. T. Boys, “Inductive power transfer,” *Proc. IEEE*, vol. 101, no. 6, pp. 1276−1289, Jun. 2013.

[2] C. C. Mi, G. Buja, S. Y. Choi, and C. T. Rim, “Modern advances in wireless power transfer systems for roadway powered electric vehicles,” *IEEE Trans. Ind. Electron.*, vol. 63, no. 10, pp. 6533−6545, Oct. 2016.

[3] M. Song, P. Jayathurathnage, E. Zanganeh *et al.*, “Wireless power transfer based on novel physical concepts,” *Nat. Electron.*, vol. 4, no. 10, pp. 707–716, Oct. 2021.

[4] D. H. Nguyen, “Electric vehicle — Wireless charging-discharging lane decentralized peer-to-peer energy trading,” *IEEE Access*, vol. 8, pp. 179616−179625, Sept. 2020.

[5] Y. Zhou, C. Liu, and Y. Huang, “Wireless power transfer for implanted medical application: A review,” *Energies*, vol. 13, no. 11, pp. 2837, Jun. 2020.

[6] W. Liu, K. T. Chau, C. C. T. Chow, and C. H. T. Lee, “Wireless energy trading in traffic internet,” *IEEE Trans. Power Electron.*, vol. 37, no. 4, pp. 4831–4841, Jan. 2022.

[7] A. Y. S. Lam, K. Leung, and V. O. K. Li, “Vehicular energy network,” *IEEE Trans. Transport. Electrific.*, vol. 3, no. 2, pp. 392−404, Jun. 2017.

[8] X. Tian, K. T. Chau, W. Liu, and C. H. T. Lee, “Selective wireless power transfer using magnetic field editing,” *IEEE Trans. Power Electron.*, vol. 36, no. 3, pp. 2710−2719, Mar. 2021.

[9] J. H. Kim, B. H. Choi, H. R. Kim, C. T. Rim, and Y. S. Kim, “Single-variable-input active sidelobe suppression method for synthesized magnetic field focusing technology and its optimization,” *IEEE Trans. Ind. Electron.*, vol. 67, no. 11, pp. 9813−9823, Nov. 2020.

[10] W. Liu, K. T. Chau, C. H. T. Lee, L. Cao, and W. Han, “Wireless power and drive transfer for piping network,” *IEEE Trans. Ind. Electron.*, vol. 69, no. 3, pp. 2345–2356, Mar. 2022.

[11] W. Liu, K. T. Chau, C. H. T. Lee, W. Han, X. Tian, and W. H. Lam, “Full-range soft-switching pulse frequency modulated wireless power transfer,” *IEEE Trans. Power Electron.*, vol. 35, no. 6, pp. 6533−6547, Jun. 2020.

[12] X. Tian, P. M. Lee, Y. J. Tan *et al.*, “Wireless body sensor networks based on metamaterial textiles,” *Nat. Electron.*, vol. 2, no. 6, pp. 243−251, Jun. 2019.

[13] W. Liu, T. Placke, and K. T. Chau, “Overview of batteries and battery management for electric vehicles,” *Energy Rep.*, vol. 8, pp. 4058–4084, Nov. 2022.

[14] R. Schmuch, R. Wagner, G. Hörpel, T. Placke, and M. Winter, “Performance and cost of materials for lithium-based rechargeable automotive batteries,” *Nat. Energy*, vol. 3, no. 4, pp. 267−278, Apr. 2018.

[15] J. Lu, G. Zhu, D. Lin, S. Wong, and J. Jiang, “Load-independent voltage and current transfer characteristics of high-order resonant network in IPT

system," *IEEE J. Emerg. Sel. Topics Power Electron.*, vol. 7, no. 1, pp. 422–436, Mar. 2019.

[16] T. Tan, K. Chen, Y. Jiang, Q. Lin, L. Yuan, and Z. Zhao, "A bidirectional wireless power transfer system control strategy independent of real-time wireless communication," *IEEE Trans. Ind. Appl.*, vol. 56, no. 2, pp. 1587−1598, Mar.−Apr. 2020.

[17] Y. Fan, Y. Sun, X. Dai, Z. Zuo, and A. You, "Simultaneous wireless power transfer and full-duplex communication with a single coupling interface," *IEEE Trans. Power Electron.*, vol. 36, no. 6, pp. 6313−6322, Jun. 2021.

[18] Z. Huang, C. S. Lam, P. I. Mak, R. P. d. S. Martins, S. C. Wong, and C. K. Tse, "A single-stage inductive-power-transfer converter for constant-power and maximum-efficiency battery charging," *IEEE Trans. Power Electron.*, vol. 35, no. 9, pp. 8973−8984, Sept. 2020.

[19] X. Qu, Y. Jing, H. Han, S. Wong, and C. K. Tse, "Higher order compensation for inductive-power-transfer converters with constant-voltage or constant-current output combating transformer parameter constraints," *IEEE Trans. Power Electron.*, vol. 32, no. 1, pp. 394−405, Jan. 2017.

[20] Y. Li, J. Hu, X. Li *et al.*, "Analysis, design and experimental verification of a mixed high order compensations-based WPT system with constant current outputs for driving multistring LEDs," *IEEE Trans. Ind. Electron.*, vol. 67, no. 1, pp. 203–213, Jan. 2020.

[21] W. Zhong and S. Y. R. Hui, "Maximum energy efficiency operation of series-series resonant wireless power transfer systems using On-Off Keying modulation," *IEEE Trans. Power Electron.*, vol. 33, no. 4, pp. 3595–3603, Mar. 2017.

[22] H. Li, S. Chen, J. Fang, Y. Tang, and M. A. d. Rooij, "A low-subharmonic, full-range, and rapid pulse density modulation strategy for ZVS full-bridge converters," *IEEE Trans. Power Electron.*, vol. 34, no. 9, pp. 8871–8881, Sept. 2019.

[23] W. Liu, K. T. Chau, C. H. T. Lee, X. Tian, and C. Jiang, "Hybrid frequency pacing for high-order transformed wireless power transfer," *IEEE Trans. Power Electron.*, vol. 36, no. 1, pp. 1157–1170, Apr. 2021.

[24] X. Li, Y. Li, C. Tsui, and W. Ki, "Wireless power transfer system with ΔΣ-modulated transmission power and fast load response for implantable medical devices," *IEEE Trans. Circuits Syst. II Exp. Briefs*, vol. 64, no. 3, pp. 279–283, Mar. 2017.

[25] S. Li, S. Lu, and C. C. Mi, "Revolution of electric vehicle charging technologies accelerated by wide bandgap devices," *Proc. IEEE*, vol. 109, no. 6, pp. 985−1003, Jun. 2021.

[26] X. Qu, H. Chu, Z. Huang *et al.*, "Wide design range of constant output current using double-sided LC compensation circuits for inductive-power-transfer applications," *IEEE Trans. Power Electron.*, vol. 34, no. 3, pp. 2364−2374, Mar. 2019.

[27] S. Li, W. Li, J. Deng, T. D. Nguyen, and C. C. Mi, "A double-sided LCC compensation network and its tuning method for wireless power transfer," *IEEE Trans. Veh. Technol.*, vol. 64, no. 6, pp. 2261–2273, Jun. 2015.

[28] Y. C. Liu, J. Zhang, C. K. Tse, C. Zhu, and S. C. Wong, "General pathways to higher order compensation circuits for IPT converters via sensitivity analysis," *IEEE Trans. Power Electron.*, vol. 36, no. 9, pp. 9897−9906, Sept. 2021.

[29] F. Lu, H. Zhang, H. Hofmann, and C. C. Mi, "A double-sided LC-compensation circuit for loosely coupled capacitive power transfer," *IEEE Trans. Power Electron.*, vol. 33, no. 2, pp. 1633−1643, Feb. 2018.

[30] J. Lu, G. Zhu, D. Lin, Y. Zhang, H. Wang, and C. C. Mi, "Realizing constant current and constant voltage outputs and input zero phase angle of wireless power transfer systems with minimum component counts," *IEEE Trans. Intell. Transp. Syst.*, vol. 22, no. 1, pp. 600–610, Jan. 2021.

[31] V. B. Vu, D. H. Tran, and W. Choi, "Implementation of the constant current and constant voltage charge of inductive power transfer systems with the double-sided LCC compensation topology for electric vehicle battery charge applications," *IEEE Trans. Power Electron.*, vol. 33, no. 9, pp. 7398–7410, Sept. 2018.

[32] X. Qu, H. Chu, S. C. Wong, and C. K. Tse, "An IPT battery charger with near unity power factor and load-independent constant output combating design constraints of input voltage and transformer parameters," *IEEE Trans. Power Electron.*, vol. 34, no. 8, pp. 7719–7727, Aug. 2019.

[33] W. Liu, K. T. Chau, X. Tian, H. Wang, and Z. Hua, "Smart wireless power transfer — opportunities and challenges," *Renew Sustain. Energy Rev.*, vol. 180, pp. 113298, Jul. 2023.

[34] Y. Liu, C. Liu, W. Wang, S. Liu, and Y. Chen, "A novel wired/wireless hybrid multi-port energy router for dynamic EV energy internet with grid-tied and islanded operations," *IEEE Trans. Ind. Electron.*, early access, 2023. DOI: 10.1109/TIE.2023.3274865.

[35] Z. Liu, Y. G. Su, Y. M. Zhao, A. P. Hu, and X. Dai, "Capacitive power transfer system with double T-type resonant network for mobile devices charging/supply," *IEEE Trans. Power Electron.*, vol. 37, no. 2, pp. 2394–2403, Feb. 2022.

[36] J. Gao, J. Zhou, C. Yuan *et al.*, "Stable wireless power transmission for a capsule robot with randomly changing attitude," *IEEE Trans. Power Electron.*, vol. 38, no. 2, pp. 2782–2796, Feb. 2023.

[37] L. Yang, X. Li, S. Liu, Z. Xu, C. Cai, and P. Guo, "Analysis and design of three-coil structure WPT system with constant output current and voltage for battery charging applications," *IEEE Access*, vol. 7, pp. 87334–87344, Jun. 2019.

Wei Liu (Senior Member, IEEE) received the B.Eng. and M.Eng. degrees in electrical engineering from China University of Petroleum, Qingdao, China, and a Ph.D. degree in electrical and electronic engineering from The University of Hong Kong (HKU), Hong Kong, China, in 2014, 2017, and 2021, respectively.

He is currently an Assistant Professor at the Research Centre for Electric Vehicles and Department of Electrical and Electronic Engineering, The Hong Kong Polytechnic University (PolyU). He has been an Honorary Assistant Professor at the Department of Electrical and Electronic Engineering, HKU, since 2023. Dr. Liu served as a Postdoctoral Fellow and then was promoted to a Research Assistant Professor at the Department of Electrical and Electronic Engineering, HKU from 2021 to 2023. He also worked as a Visiting Researcher with Nanyang Technological University, Singapore (NTU), in 2019. His research interests include wireless power transfer, power electronics, biomedical power electronics, and electric vehicle technologies.

Dr. Liu was the recipient of the Power Engineering Prize from HKU, the Excellent Paper Award, and the Best Presentation Award from international conferences in the area of Electric Vehicles and Transportation Electrification. He is also a Guest Associate Editor of *IEEE Journal of Emerging and Selected Topics in Power Electronics (JESTPE)*, Associate Editor of international journals, and Session Chair of international conferences.

Jianghua Lu (Member, IEEE) received the M.S. and Ph.D. degrees from the Wuhan University of Technology, Wuhan, China, in 2016 and 2020, respectively.

From September 2018 to October 2020, he was a joint Ph.D. student funded by the China Scholarship Council with the Department of Electrical and Computer Engineering, San Diego State University, San Diego, CA, USA. He is currently a Lecturer at School of Information Science and Engineering, Wuhan University of Science and Technology. His research interests include wireless power transfer and resonant converters.

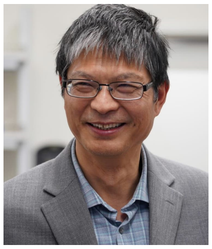

Chunting Chris Mi (Fellow, IEEE) received the B.S.E.E. and M.S.E.E. degrees from Northwestern Polytechnical University, Xi'an, China, and the Ph.D. degree from the University of Toronto, Toronto, ON, Canada, in 1985, 1988, and 2001, respectively, all in electrical engineering.

He is a Professor and the Chair of electrical and computer engineering and the Director with the Department of Energy (DOE)–funded Graduate Automotive Technology Education (GATE) Center for Electric Drive Transportation, San Diego State University, San Diego, CA, USA. Prior to joining SDSU, he was with the University of Michigan, Dearborn, MI, USA, from 2001 to 2015. His research interests include electric drives, power electronics, electric machines, electrical and hybrid vehicles, wireless power transfer, and power electronics.

Dr. Mi was a recipient of the IEEE PELS Emerging Technology Award in 2019, IEEE Transaction on Power Electronics Best Paper Award, and two IEEE Transaction on Power Electronics Prize Letter Awards. He is a Fellow of both IEEE and SAE.

K. T. Chau (Fellow, IEEE) received the B.Sc. (Eng.), M.Phil., and Ph.D. degrees in electrical and electronic engineering from The University of Hong Kong, Hong Kong, in 1988, 1991, and 1993, respectively. Currently, he serves as Chair Professor of Electrical Energy Engineering at the Research Centre for Electric Vehicles and Department of Electrical and Electronic Engineering, The Hong Kong Polytechnic University. His research interests include electric and hybrid vehicles, power electronics and drives, and renewable energies. He is the author of nine books and more than 350 journal papers.

Prof. Chau is a Fellow of the Institution of Engineering and Technology (IET), U.K., and of the Hong Kong Institution of Engineers. He is also a Co-editor of the Journal of Asian Electric Vehicles. He is a Chartered Engineer. He was the recipient of the Changjiang Chair Professorship from the Ministry of Education, China, and the Environmental Excellence in Transportation Award for Education, Training, and Public Awareness from the Society of Automotive Engineers International.